Supplementary Material of

Structural and lattice-dynamical properties of Tb_2O_3 under compression: a comparative study with rare-earth and related sesquioxides

Jordi Ibáñez,[1] Juan Ángel Sans,[2] Vanesa Cuenca-Gotor,[2] Robert Oliva,[3*] Óscar Gomis,[4] Plácida Rodríguez-Hernández,[5] Alfonso Muñoz,[5] Ulises Rodríguez-Mendoza,[5] Matías Velázquez,[6] Philippe Veber,[6,7] Catalin Popescu[8] and Francisco Javier Manjón[2*]

[1]*Institute of Earth Sciences Jaume Almera, MALTA Consolider Team, Consell Superior d'Investigacions Científiques, 08028 Barcelona, Catalonia, Spain*

[2]*Instituto de Diseño para la Fabricación y Producción Automatizada, MALTA Consolider Team, Universitat Politècnica de València, 46022 València, Spain*

[3]*Faculty of Fundamental Problems of Technology, Wroclaw University of Science and Technology, 50-370, Wrocław, Poland*

[4]*Centro de Tecnologías Físicas, MALTA Consolider Team, Universitat Politècnica de València, 46022 València, Spain*

[5]*Departamento de Física, Instituto de Materiales y Nanotecnología, MALTA Consolider Team, Universidad de La Laguna, 38200 San Cristóbal de la Laguna, Tenerife, Spain*

[6]*Univ. Grenoble Alpes, CNRS, Grenoble INP, SIMAP, 38000 Grenoble, France.*

[7]*CNRS, Institut Lumière Matière, Université Claude Bernard Lyon 1, UMR5306, 69622 Villeurbanne, France*

[8]*ALBA-CELLS, MALTA Consolider Team, 08290 Cerdanyola del Vallès (Barcelona), Catalonia, Spain.*

*Corresponding authors: robert.oliva.vidal@pwr.edu.pl; fjmanjon@fis.upv.es

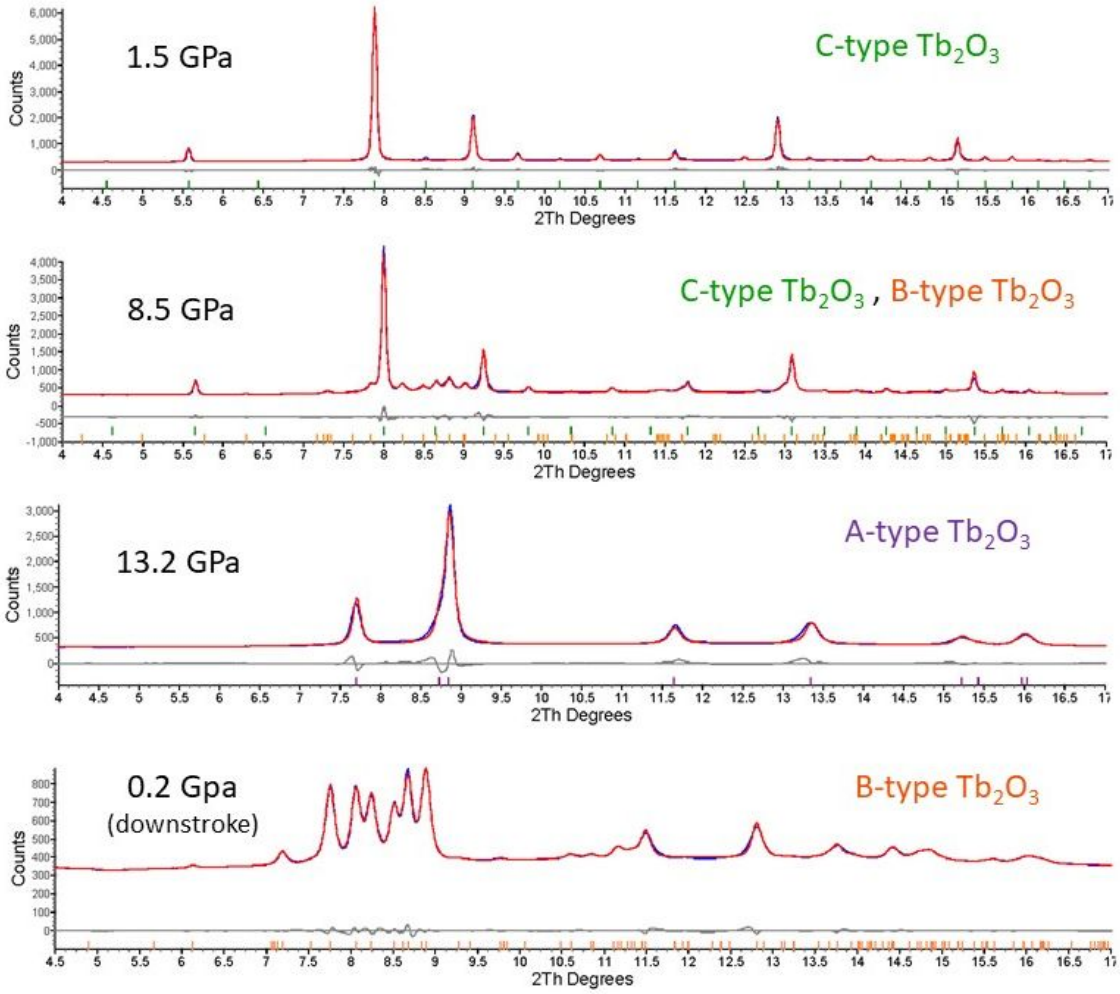

Figure S1: Selected examples of calculated and difference profiles obtained from full-pattern matching refinements to the experimental XRD scans. For C-type Tb_2O_3, Rietveld refinements were carried out. For the high-pressure polymorphs, the Pawley/Le Bail methods were used.

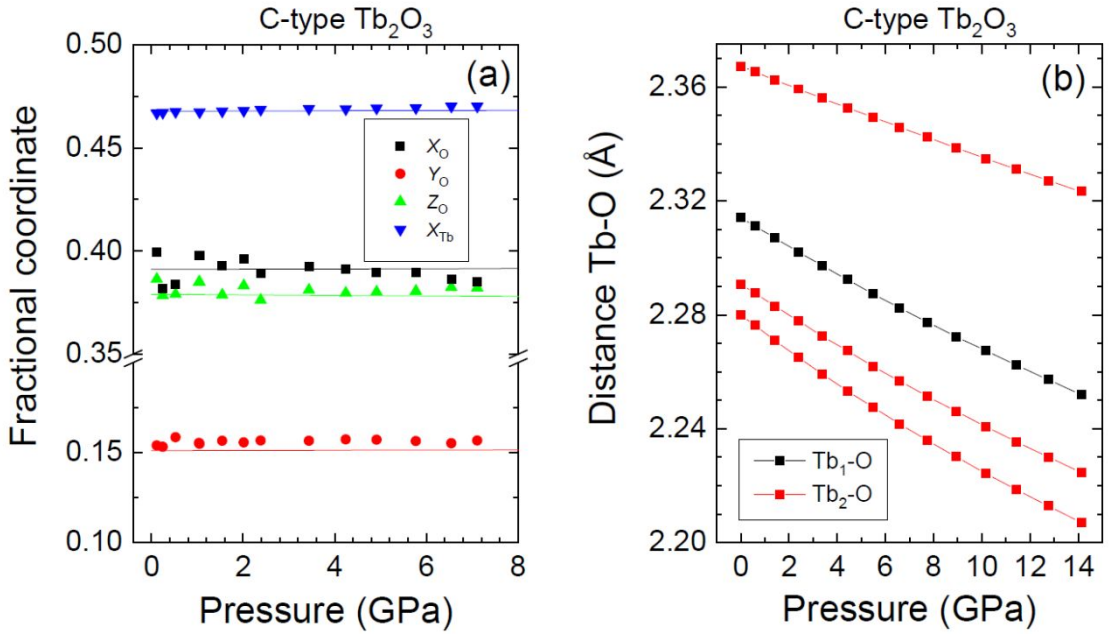

Figure S2: (a) Experimental (symbols) and theoretical (lines) pressure dependence of the four free atomic parameters in C-type Tb_2O_3. The calculated error for the experimental values is smaller than (of the order of) the size of the symbols for Tb (O) coordinates. (b) Theoretical pressure dependence of the Tb-O distances in C-type Tb_2O_3.

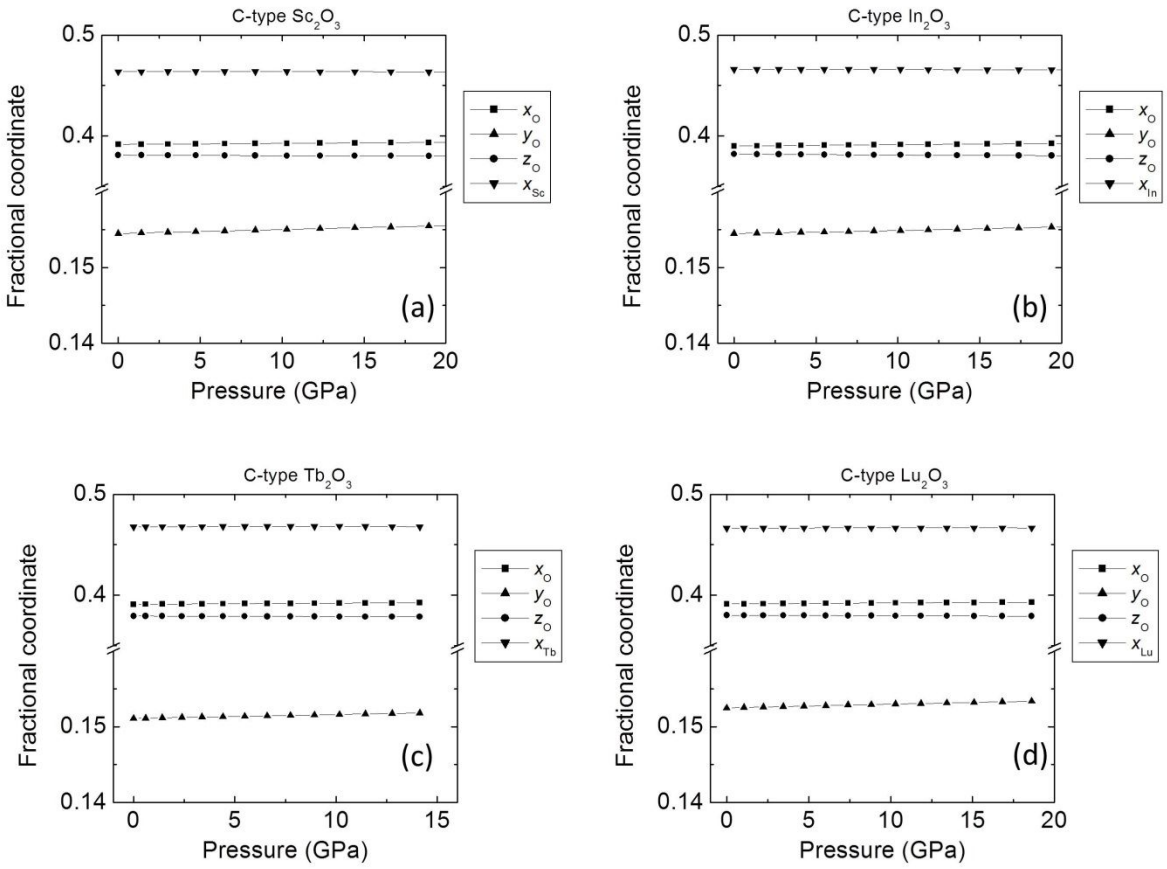

Figure S3: Theoretical pressure dependence of the four free atomic parameters in several C-type sesquioxides: (a) In_2O_3, (b) Sc_2O_3, (c) Tb_2O_3, and (d) Lu_2O_3.

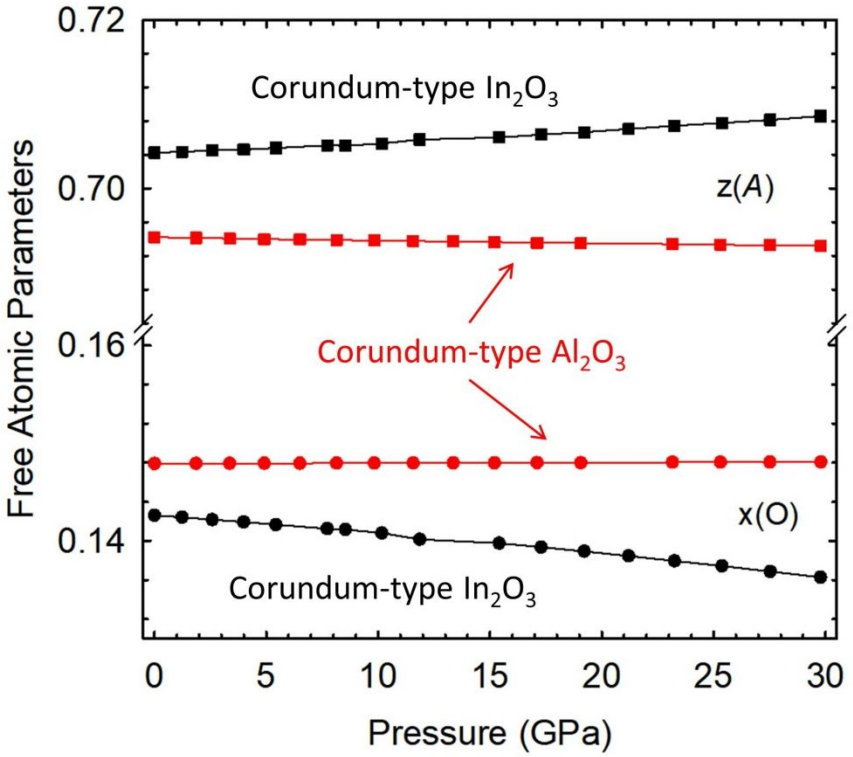

Figure S4: Theoretical pressure dependence of the four free atomic parameters in corundum-type In_2O_3 and Al_2O_3.

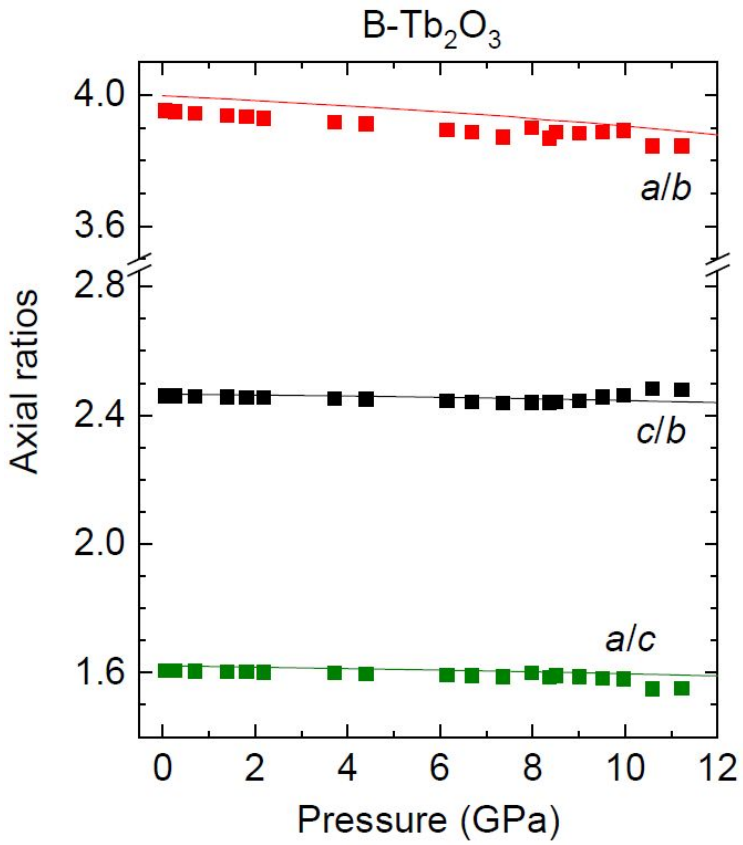

Figure S5: Experimental (symbols) and theoretical (lines) pressure dependence of the *c*/*b*, *a*/*b* and *a*/*c* axial ratios in B-type Tb_2O_3.

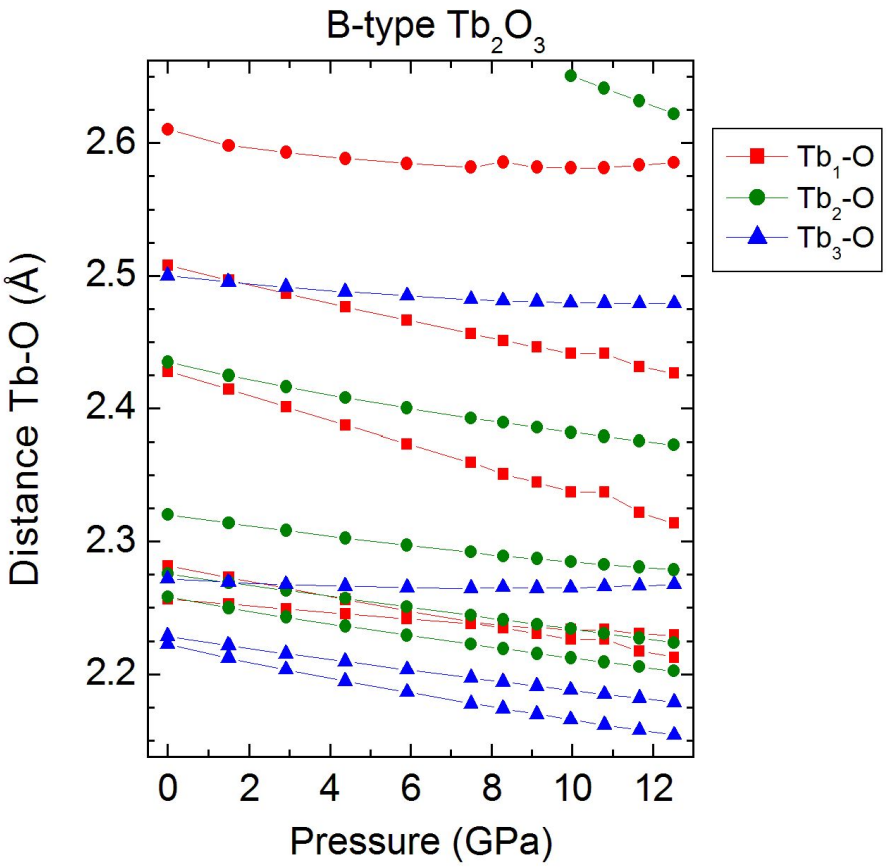

Figure S6: Theoretical pressure dependence of the Tb-O distances in B-type Tb_2O_3.

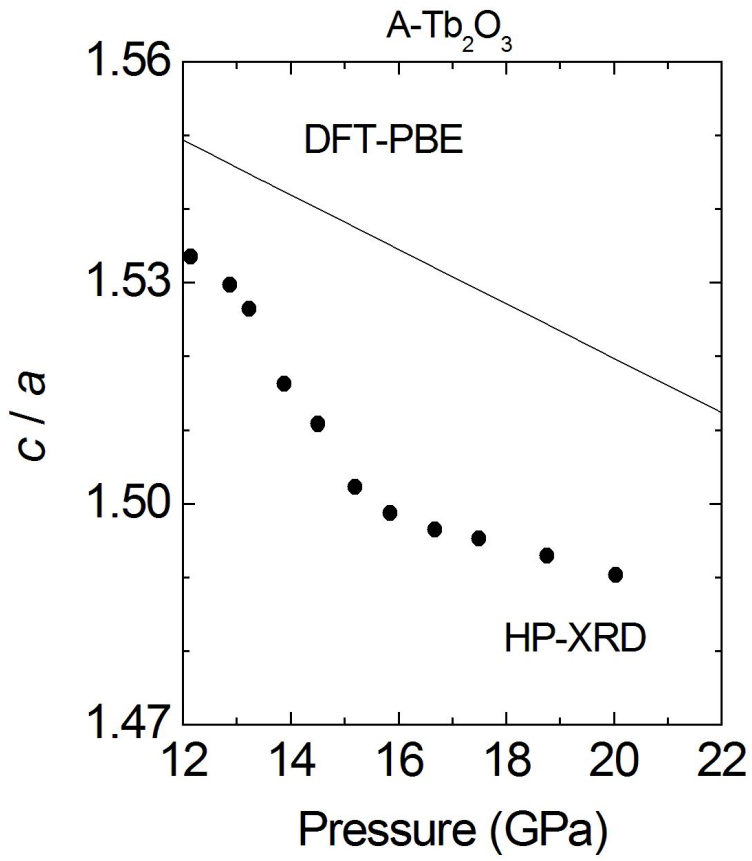

Figure S7: Experimental (symbols) and theoretical (lines) pressure dependence of the *c/a* axial ratio in A-type Tb_2O_3.

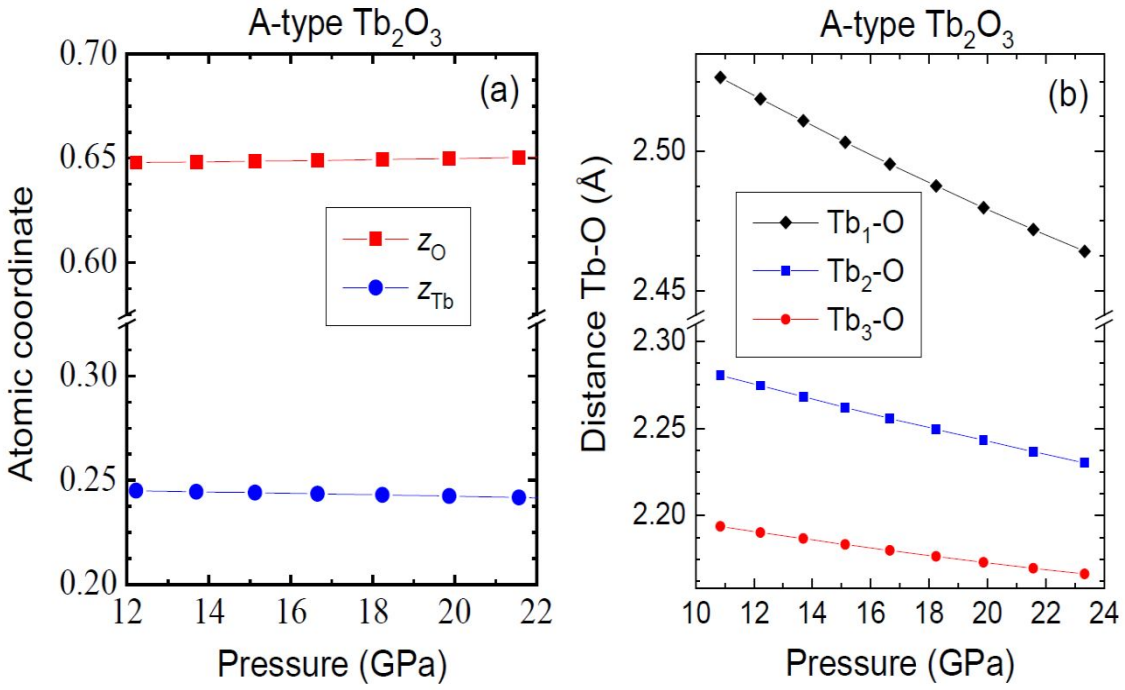

Figure S8: (a) Theoretical pressure dependence of the two free atomic parameters of A-type Tb_2O_3. (b) Theoretical pressure dependence of the Tb-O distances in A-type Tb_2O_3.

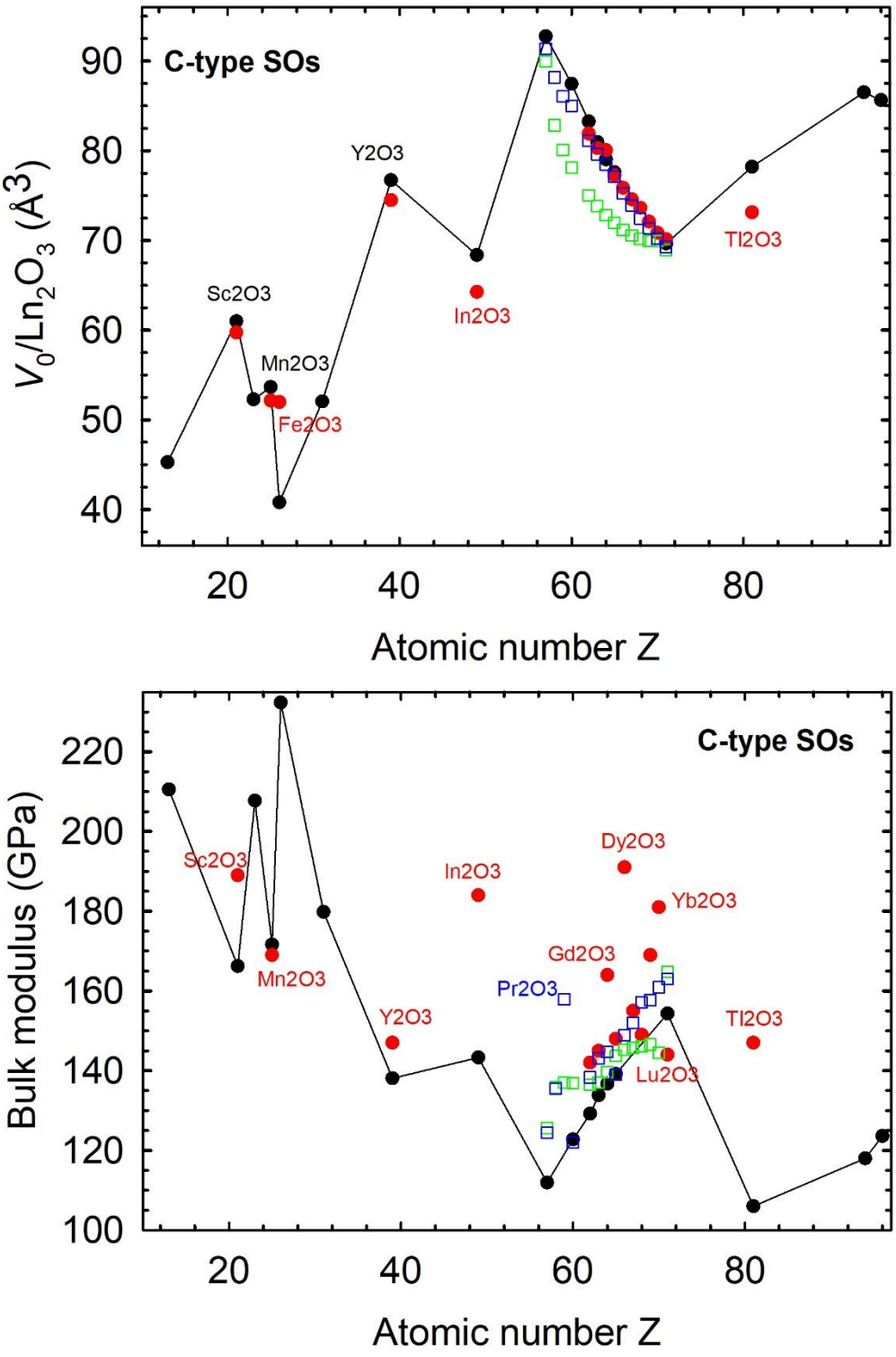

Figure S9: Circles represent the experimental (red, from Table S1) and theoretical (black, from Table S2) volume per formula unit (a) and bulk modulus (b) of C-type sesquioxides vs. the atomic number Z. Theoretical data of Ref. 34 with WC-GGA (green open squares) and GGA+U (blue open squares) are also shown for comparison.

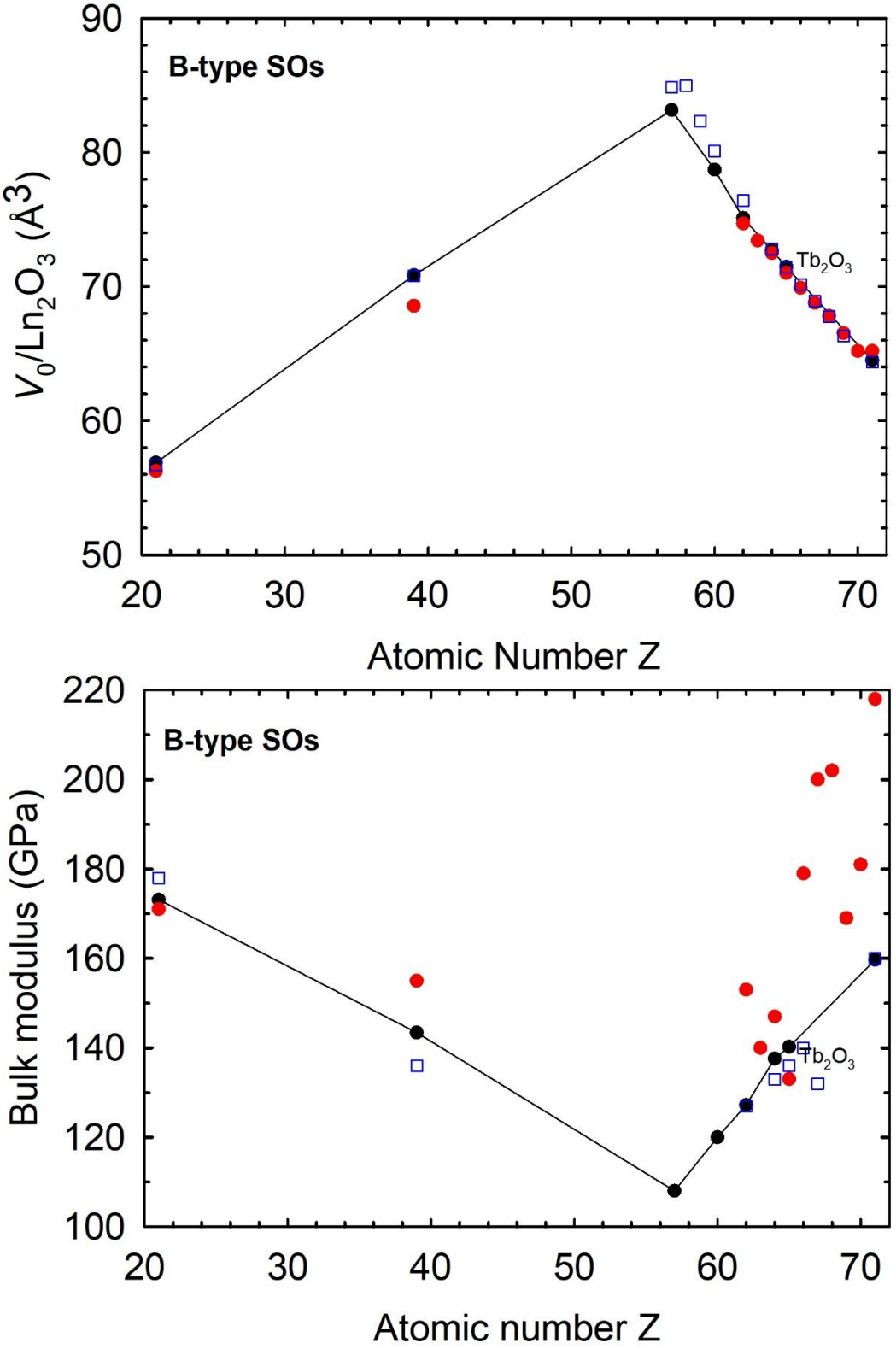

Figure S10: Circles represent the experimental (red, from Table S1) and theoretical (black, from Table S2) volume per formula unit (a) and bulk modulus (b) of B-type sesquioxides vs. the atomic number Z. Theoretical data of Ref. 32 (blue open squares) are also shown for comparison.

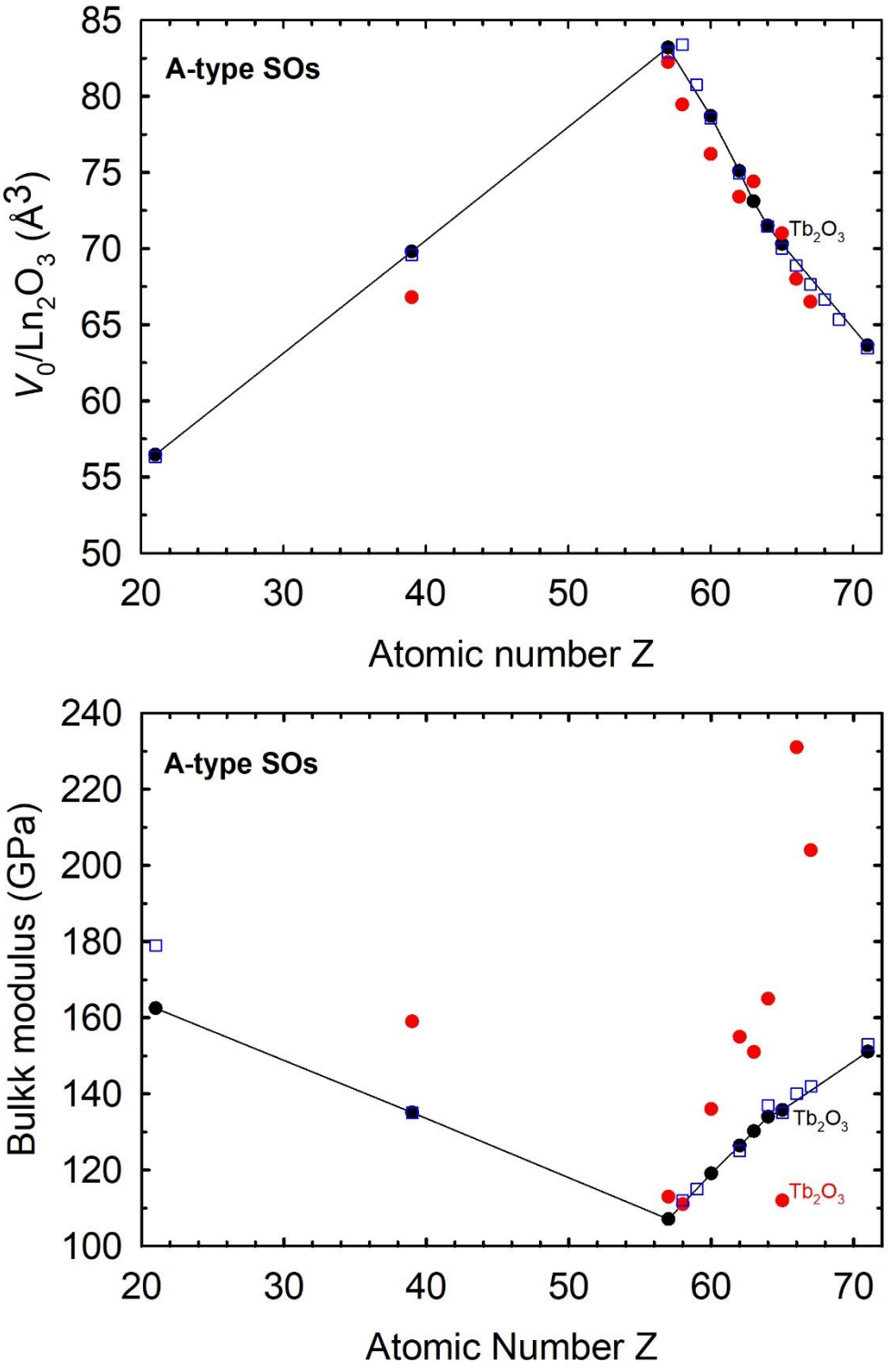

Figure S11: Circles represent the experimental (red, from Table S1) and theoretical (black, from Table S2) volume per formula unit (a) and bulk modulus (b) of A-type sesquioxides vs. the atomic number Z. Theoretical data of Ref. 32 (blue open squares) are also shown for comparison.

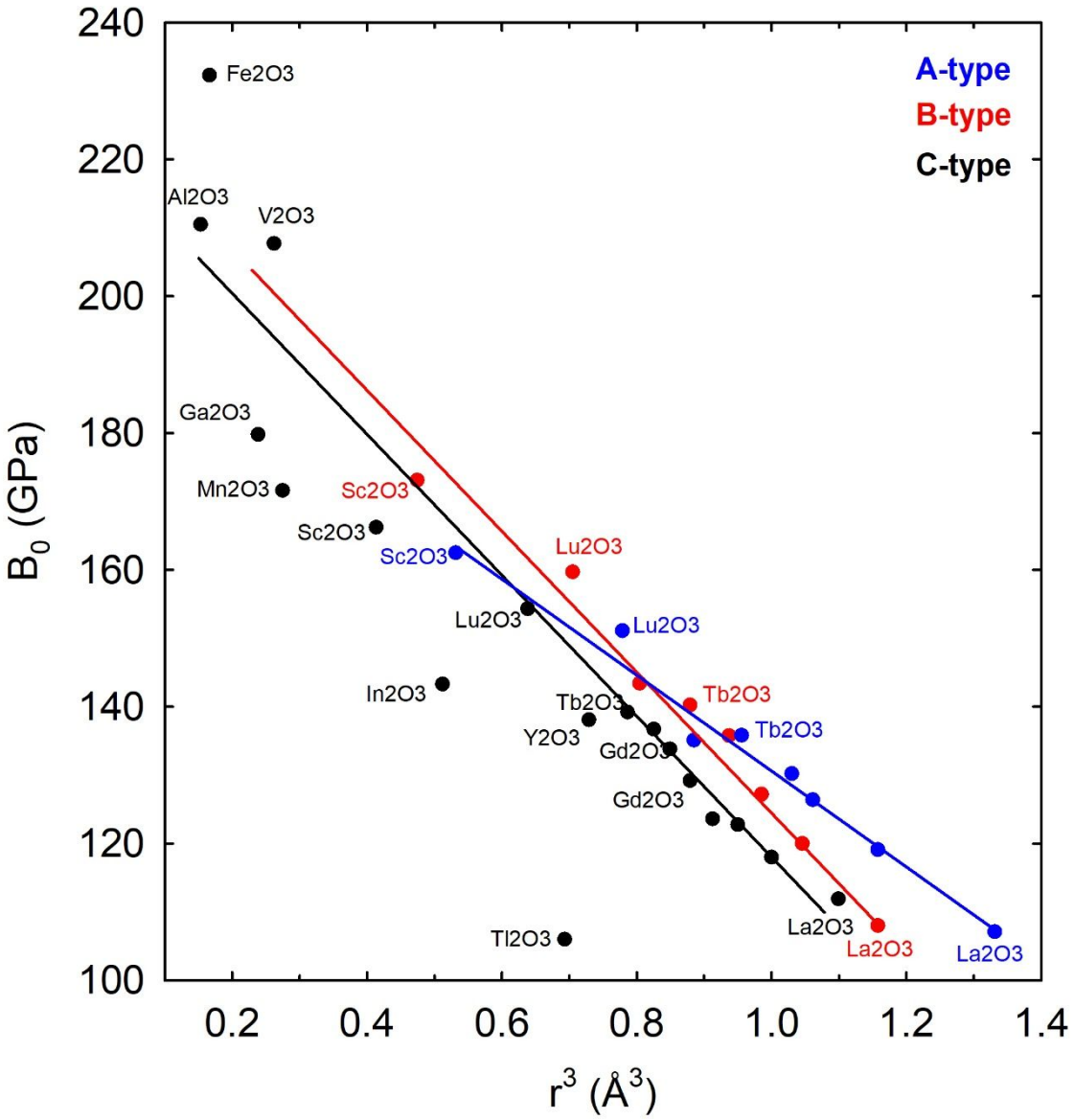

Figure S12: Theoretical (symbols) bulk modulus of C-type (black), B-type (red), and A-type (blue) RE-SOs as a function of the third power of the cation ionic radius (r^3). Cation ionic radii have been taken from Ref. [119] for valence 3+ with 6-, 6.5-, and 7-fold coordination for C-, B-, and A-type crystalline structures.

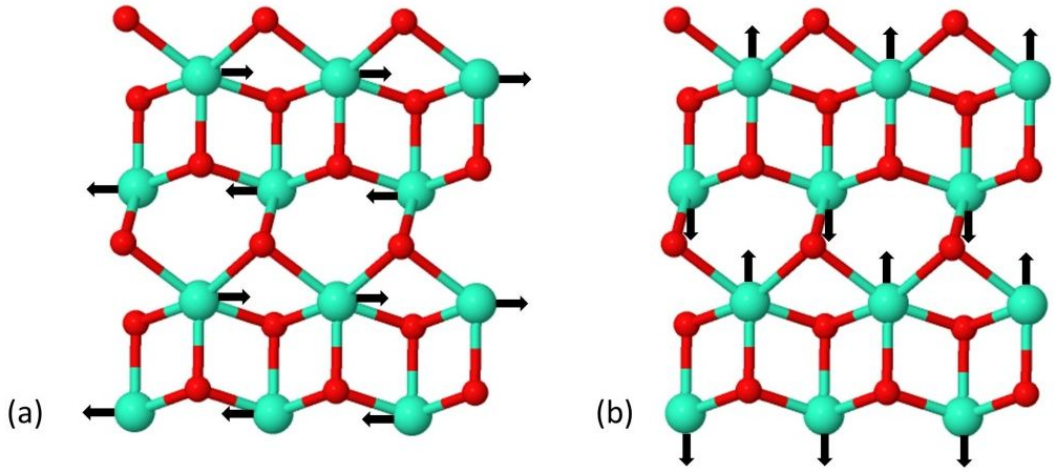

Figure S13: Atomic vibrations of the (a) low-wavenumber E_g^1 mode and (b) low-wavenumber A_{1g}^1 modes in A-type Tb_2O_3. Big blue atoms are Tb and small red atoms are O. The vertical direction corresponds to the hexagonal c axis and the horizontal direction is perpendicular to the (110) direction of the hexagonal unit cell. Figures have been drawn with the help of J-ICE program **[40]**.

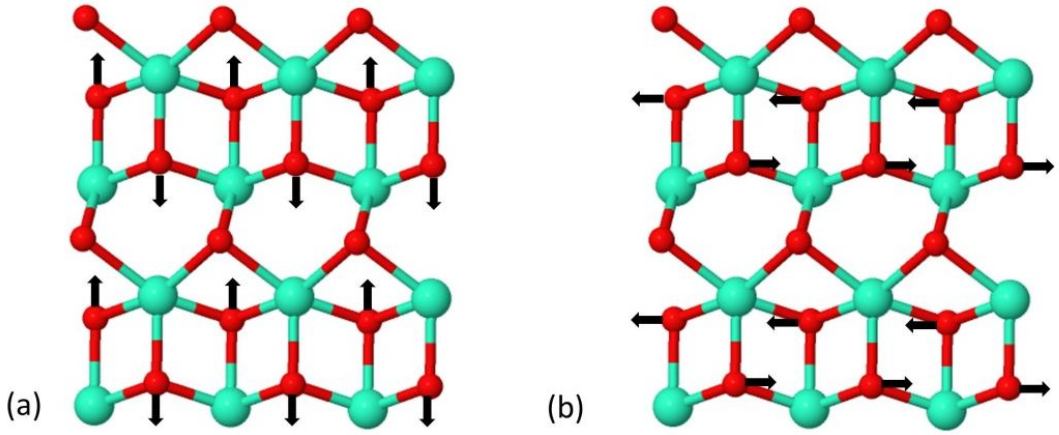

Figure S14: Atomic vibrations of the (a) high-wavenumber A_{1g}^2 mode and (b) high-wavenumber E_g^2 modes in A-type Tb_2O_3. Big blue atoms are Tb and small red atoms are O. The vertical direction corresponds to the hexagonal c axis and the horizontal direction is perpendicular to the (110) direction of the hexagonal unit cell. Figures have been drawn with the help of J-ICE program **[40]**.

Table S1: Experimental data of the equation of state for Ln_2O_3 and related sesquioxides having a C-type (or bixbyite) phase, a B-type and an A-type phase. Compounds are ordered on increasing volume per formula unit of the different phases.

	Phase	V_0 (Å^3)	B_0 (GPa)	B_0'	Ref.
Fe_2O_3	C (exp)	51.97			[1]
Mn_2O_3	C (exp)	52.2	169	7.3	[2]
Sc_2O_3	C (exp)	59.7	189	4	[3]
	B (exp)	55.1	216	5 (fixed)	
	C (exp)	60.8	154	7 (fixed)	[4]
	B (exp)		180	4 (fixed)	
	C (exp)	59.6	198	4 (fixed)	[5]
	C (exp)	59.6	223	1.65	
	B (exp)	56.2	171	4 (fixed)	
	B (exp)	57.0	141.6	4.8	
In_2O_3	C (exp)	64.9	194	4.8 (fixed)	[6]
	C (exp)	64.7	179	5.15	[7]
	C (exp)	64.3	184	4 (fixed)	[8]
Lu_2O_3	C (exp)	70.1	214	9	[9]
	B (exp)	65.2	218	2.3	
	C (exp)	70.1	114	1.7	[10]
	C (exp)	70.1	144	6.7	[11]
Yb_2O_3	C (exp)	70.8	181	7.3	[12]
	B (exp)	65.2	181	1.3	
Tm_2O_3	C (exp)	72.1	149	4.8	[13]
	B (exp)	66.5	169	4 (fixed)	
Tl_2O_3	C (exp)	73.1	147	5	[14]
Er_2O_3	C (exp)	73.5	200	8.4	[15]
	B (exp)	67.8	202	1.0	
	C (exp)	73.3	136	5.9	[11]
	C (exp)	73.6	148.8	4.02	[16]
Y_2O_3	C (exp)	74.4	146	5.5	[11]
	C (exp)	74.5	147	4 (fixed)	[17]
	B (exp)	68.6	155	4 (fixed)	
	A (exp)	66.8	159	4 (fixed)	
	B (exp)	69.0	159	4 (fixed)	[18]
	A (exp)	67.8	156	4 (fixed)	

	Phase	V_0 (Å^3)	B_0 (GPa)	B_0'	Ref.
Ho_2O_3	C (exp)	74.6	206	4.8	[19]
	B (exp)	68.8	200	2.1	
	A (exp)	66.5	204	3.8	
	C (exp)		155	4 (fixed)	[20]
	A (exp)		249	4 (fixed)	
Dy_2O_3	C (exp)	75.9	191	2.8	[21]
	B (exp)	69.9	179	4.2	
	A (exp)	68.0	231	3.5	
Tb_2O_3	C (exp)	77.3	148	2.1(4)	This work
	B (exp)	71.0	133	4 (fixed)	
	A (exp)	71.0	112	4 (fixed)	
Gd_2O_3	C (exp)		188	4 (fixed)	[22]
	A (exp)		160	4 (fixed)	
	C (exp)		134	4 (fixed)	[23]
	B (exp)	72.5	147	4 (fixed)	
	A (exp)		174	4 (fixed)	
	C (exp)	79.0	125	4.7	[11]
	C (exp)	80.1	164	4	[24]
Eu_2O_3	C (exp)	80.3	145	4	[25]
	A (exp)	74.4	151	4	
	C (exp)	80.0	115	5.9	[11]
	C (exp)		140	4 (fixed)	[20]
	A (exp)		155	4 (fixed)	
	B (exp)	73.4	140	4 (fixed)	[26]
Sm_2O_3	C (exp)	81.9	142	4	[27]
	A (exp)	72.1	224	1.5	
	C (exp)	81.7	116	4 (fixed)	[11]
	A (exp)	73.0	130	6.9	
	C (exp)	81.6	149	4 (fixed)	[28]
	B (exp)	74.7	153	4 (fixed)	
	A (exp)	73.4	155	4 (fixed)	
Nd_2O_3	A (exp)		136	4 (fixed)	[29]
	A (exp)	76.2	142	4 (fixed)	[30]
Ce_2O_3	A (exp)	79.5	111	4.7	[31]
La_2O_3	A (exp)	82.2	113	6.0	[11]

Table S2: Theoretical data of the equation of state for some Ln_2O_3 and related sesquioxides having a C-type (or bixbyite) phase, a B-type and an A-type phase. Compounds are ordered on increasing volume per formula unit of the different phases.

	Phase	V_0 (Å^3)	B_0 (GPa)	B_0'	Ref.
Al_2O_3	C (the)	45.3	210.5	4.1	This work
Ga_2O_3	C (the)	52.1	179.8	4.4	This work
V_2O_3	C (the)	52.3	207.7	4.2	This work
Mn_2O_3	C (the)	53.7	171.6	4.8	This work
Sc_2O_3	C (the)	61.0	166.2	4.2	This work
	B (the)	56.9	173.1	3.9	This work
	A (the)	56.5	162.5	4.1	This work
In_2O_3	C (the)	68.4	143.3	4.7	This work
Lu_2O_3	C (the)	69.7	154.3	4.3	This work
	B (the)	64.5	159.7	3.6	This work
	A (the)	63.6	151.1	4.0	This work
Tl_2O_3	C (the)	78.2	106	5.1	This work
Y_2O_3	C (the)	76.7	138.1	4.2	This work
	B (the)	70.8	143.4	3.1	This work
	A (the)	69.8	135.1	3.8	This work
Tb_2O_3	C (the)	77.5	139.2	4.3	This work
	C (the)	77.3	145.2		[31]
	B (the)	71.5	140.2	3.3	This work
	B (the)	71.4	137	3.5	[32]
	A (the)	70.3	135.8	3.9	This work
	A (the)	70.0	136	3.5	[32]
Gd_2O_3	C (the)	79.0	136.7	4.4	This work
	B (the)	72.7	137.6	3.0	This work
	A (the)	71.5	134.0	3.8	This work
Eu_2O_3	C (the)	81.0	133.8	4.4	This work
	B (the)	74.5	135.8	2.0	This work
	A (the)	73.1	130.2	4.0	This work
Sm_2O_3	C (the)	83.2	129.2	4.5	This work
	B (the)	75.1	127.2	3.8	This work
	A (the)	75.1	126.4	3.8	This work
Nd_2O_3	C (the)	87.5	122.7	4.5	This work
	B (the)	78.7	120.0	3.8	This work
	A (the)	78.7	119.1	3.9	This work
La_2O_3	C (the)	92.8	111.9	4.3	This work
	B (the)	83.2	108.0	3.8	This work
	A (the)	83.2	107.1	3.9	This work

Table S3: Experimental zero-pressure wavenumbers (in cm^{-1}) and linear pressure coefficients (in $cm^{-1}GPa^{-1}$) for the Raman-active modes in several C-type SOs.

	In_2O_3[a]		Lu_2O_3[b]		Tm_2O_3[c]		Y_2O_3[d]		Tb_2O_3[e]	
Sym	ω_0	$d\omega/dP$	ω_0	$d\omega/dP$	ω_0	$d\omega/dP$	ω_0	$d\omega/dP$	ω_0	$d\omega/dP$
F_g^1	108	0.07	97	0.09	99	0.01			95	−0.25
F_g^2	118	0.4					128	-0.02	106	−0.24
A_g^1	131	1.0	119	0.54	120	0.5			119	0.68
F_g^3	152	1.4	136	0.80					134	0.87
E_g^1	169	0.8	146	0.77			163	0.67	144	0.78
F_g^4	205	1.3								
F_g^5	211	3.0								
F_g^6	306	2.4								
F_g^7			332	2.51			317	2.24		
E_g^2					337	2.66	330	2.77	320	2.86
F_g^8	365	4.3								
A_g^2	306	4.0	350	2.61						
F_g^9					383	3.66	377	3.60	367	3.86
E_g^3	396	3.3								
F_g^{10}			395	3.02						
A_g^3	495	3.7			425	4.32	426	5.58	405	4.33
F_g^{11}	467		457	3.50						
F_g^{12}	513		503	4.46	484	4.65	469	4.63	452	4.76
F_g^{13}										
A_g^4										
E_g^4	590	5.2	598	2.06						
F_g^{14}	628	6.0	618	4.21	603	4.51	594	4.51	576	4.76

[a]Ref. 8, [b]Ref. 9, [c]Ref. 13, [d]Ref. 35, [e]This work.

Table S4: Theoretical zero-pressure wavenumbers (in cm^{-1}) and linear pressure coefficients (in $cm^{-1}GPa^{-1}$) for the Raman-active modes in several C-type SOs.

	In_2O_3[a]		Yb_2O_3[b]		Dy_2O_3[c]		Tb_2O_3[c]		Gd_2O_3[c]	
Sym	ω_0	$d\omega/dP$	ω_0	$d\omega/dP$	ω_0	$d\omega/dP$	ω_0	$d\omega/dP$	ω_0	$d\omega/dP$
F_g^1	106	0.01			95.02	0.12	95.05	−0.06	94.60	0.13
F_g^2	114	0.30			98.40	0.46	98.36	0.36	97.85	0.48
A_g^1	128	0.80	114	0.97	114.10	1.06	114.29	0.96	114.00	1.18
F_g^3	148	1.20			131.80	1.25	132.35	1.13	132.30	1.36
E_g^1	165	1.10			142.70	0.96	143.13	0.93	142.90	1.04
F_g^4	204	1.50			170.90	1.70	171.36	1.70	171.10	1.89
F_g^5	211	3.00			176.90	1.57	177.48	1.52	177.30	1.73
F_g^6	302	2.20			299.30	2.48	295.32	2.61	292.20	2.71
F_g^7	312	2.60			305.00	2.41	300.68	2.57	297.10	2.63
E_g^2	308	3.10	332	3.30	315.10	3.23	311.07	3.32	307.70	3.49
F_g^8	356	3.90			334.00	4.34	330.57	4.33	327.60	4.67
A_g^2	302	3.10			348.40	3.15	345.04	2.92	342.20	3.18
F_g^9	379	3.90	379	4.17	363.80	4.24	360.67	4.26	357.80	4.62
E_g^3	385	3.60			368.80	4.60	365.13	4.74	362.20	5.00
F_g^{10}	438	3.00			377.70	4.29	372.74	4.08	368.30	4.64
A_g^3	476	3.40	430	4.35	402.70	4.75	396.77	5.08	391.30	5.37
F_g^{11}	447	4.30			416.30	3.77	411.15	4.44	406.60	4.10
F_g^{12}	499	5.00	475	5.10	448.30	5.11	442.06	5.32	436.60	5.52
F_g^{13}	520	4.70			509.70	4.00	505.15	4.28	501.30	4.28
A_g^4	576	5.40			547.70	4.27	541.45	4.51	536.40	4.55
E_g^4	565	5.20			544.30	4.65	548.42	4.83	543.50	5.00
F_g^{14}	600	5.40	595	5.16	570.10	5.17	563.49	5.30	558.00	5.60

[a] Ref. 8, [b] Ref. 36, [c] This work

Table S5: Experimental zero-pressure wavenumbers (in cm^{-1}) and linear pressure coefficients (in $cm^{-1}GPa^{-1}$) for the Raman-active modes in several B-type Ln_2O_3 compounds.

	Lu_2O_3[a]		Tm_2O_3[b]		Tb_2O_3[c]		Sm_2O_3[d]	
Sym.	ω_0	$d\omega/dP$	ω_0	$d\omega/dP$	ω_0	$d\omega/dP$	ω_0	$d\omega/dP$
B_g^1			69	0.66	70.3	0.70		
A_g^1			84	0.78	82.9	0.01	80	0.83
B_g^2	99	0.58	98	1.06	96.8	1.16	95	1.62
A_g^2	113	0.53	113	0.76	110.8	0.64	108	1.12
A_g^3			128	0.68				
B_g^3	128	0.29			122.9	0.13	118	1.15
A_g^4	167	0.73	155	1.83	156.3	0.88	144	1.67
A_g^5	174	1.56	171	1.94	172.8	2.14	175	3.03
A_g^6					216.5	1.8	219	2.32
A_g^7	285	0.81			261.8	−0.23	244	1.42
A_g^8	313	2.07	285	4.36	265.2	5.09	254	6.19
B_g^4			321	5.38	306.6	5.12	300	4.30
B_g^5	351	2.40			368.6	1.73		
A_g^9							345	5.30
A_g^{10}					391.7	3.77		
B_g^6	427	2.19	415	3.42				
A_g^{11}	458	2.53	451	3.61	426.2	2.43	421	3.3
B_g^7	464	2.41	479	2.71	446.0	2.95		
A_g^{12}	540	2.36	524	2.30	492.0	3.59	462	4.00
A_g^{13}			611	3.71			558	5.10
A_g^{14}	640	2.01	628	3.31	596.7	3.92	570	4.80

[a] Ref. 9, [b] Ref. 13, [c] This work [d] Ref. 21.

Table S6: Experimental wavenumbers (in cm^{-1}) and linear pressure coefficients (in $cm^{-1}GPa^{-1}$) for the Raman-active phonon modes in several A-type Ln_2O_3 compounds. Note that the frequencies correspond to different pressures.

	Y_2O_3 [a]		Tb_2O_3 [b]		Sm_2O_3 [c]		Nd_2O_3[e]		La_2O_3[f]	
Sym.	ω	$d\omega/dP$	ω	$d\omega/dP$	ω	$d\omega/dP$	ω	$d\omega/dP$	ω	$d\omega/dP$
E_g^1	174	0.97	116	1.40	108	0.89	107	1.03	104	0.90
A_{1g}^1	320	1.02	208	2.07	198	1.32	193	2.07	190	2.19
A_{1g}^2	527	2.10	490	2.32	450	1.43[c],2.00[d]	427	1.77	408	1.47
E_g^2	577	3.39	529	2.79	473	1.84 [c],3.40[d]	437	3.33	418	3.23

[a] Estimated from Ref. 35 (22 GPa), [b] This work (11 GPa), [c] Ref. 28 (2 GPa), [d] Ref. 37 Hongo (3 GPa), [e] Ref. 30 (0 GPa), [f] Ref. 11 (0 GPa)

Table S7: Experimental wavenumbers at 0 GPa, ω_0 (in cm^{-1}), for the Raman-active modes in several A-type Ln_2O_3 compounds. Our theoretical wavenumbers for Raman-active modes in A-type Tb_2O_3 at 0 GPa are noted in parenthesis.

	Y_2O_3[a]	Tb_2O_3[b]		Sm_2O_3[c]	Nd_2O_3[d]	Pr_2O_3[e]	Ce_2O_3[f]	La_2O_3[e]
Sym.	ω_0	ω_0	ω_0	ω_0	ω_0	ω_0	ω_0	ω_0
E_g^1	153	99	(102)	106	107	104	103	104
A_{1g}^1	298	183	(185)	195	193	187	189	190
A_{1g}^2	481	465	(455)	447	427	406		400
E_g^2	502	498	(483)	469	437	413	409	408
$\Delta\omega$	21	33		22	10	7		8
c/a	1.617[g]	1.577[g]		1.572	1.567	1.558	1.557	1.555

[a] Estimated from Ref. 35, [b] Estimated from this work, [c] Estimated from Ref. 28, [d] Ref. 30, [e] Ref. 38, [f] Ref. 39, [g] Theoretical values at 0 GPa from Ref. 33.

Table S8: Theoretical wavenumbers ω_0 (in cm^{-1}) at 0 GPa for the vibrational modes in A-type Tb_2O_3.

Mode	E_g^1	A_{1g}^1	E_u^1	A_{2u}^1	E_u^2	A_{1g}^2	A_{2u}^2	E_g^2
ω_0	*101.7*	*184.8*	*193.8*	*221.6*	*437.1*	*455.0*	*467.1*	*483.0*

Calculation of the experimental and theoretical compressibility tensor of B-type Tb_2O_3 at different pressures

The isothermal compressibility tensor, β_{ij}, is a symmetric second rank tensor that relates the state of strain of a crystal to the change in pressure that induced the deformation **[41]**. The tensor coefficients for a monoclinic crystal with *b* as the unique crystallographic axis are:

$$\beta_{ij} = \begin{pmatrix} \beta_{11} & 0 & \beta_{13} \\ 0 & \beta_{22} & 0 \\ \beta_{13} & 0 & \beta_{33} \end{pmatrix}$$

We have obtained the isothermal compressibility tensor coefficients for monoclinic B-type Tb_2O_3 at several pressures using the IRE (Institute of Radio Engineers) convention for the orthonormal basis for the tensor: $e_3||c$, $e_2||b^*$, $e_1||e_2 \times e_3$. The tensor has been obtained with the finite Eulerian approximation as implemented in the Win_Strain package **[42]**.

The change of the β monoclinic angle (always perpendicular to the *b* axis) with pressure implies that, in this monoclinic compound, the direction of the *a* axis changes with pressure assuming both *b* and *c* axis constant. Furthermore, the departure of this monoclinic angle from 90º indicates that the direction of maximum compressibility is not exactly that of the *a* axis. Therefore, in order to evaluate the direction of maximum compressibility as a function of pressure we have calculated and diagonalized the experimental and theoretical isothermal compressibility tensor, β_{ij}, at different pressures.

The experimental and theoretical elements of this tensor at different pressures are reported in **Tables S9** and **S10**, up to 11.0 GPa, where the directions of the maximum, intermediate and minimum compressibility and the values of the compressibility along

those directions are given by the eigenvectors (ev_i, i=1-3) and eigenvalues (λ_i, i=1-3), respectively.

First of all, we have to note that there is a reasonable good agreement between the experimental and calculated axial compressibilities (β_{ii} coefficients) at room pressure because $\beta_{11} > \beta_{33} > \beta_{22}$ in both cases. This result shows that the compressibility along the *a*-axis is greater than those to the *c*-axis and *b*-axis. A diagonalization of the β_{ij} tensor at room pressure yields for our experiments the maximum, intermediate and minimum compressibilities $3.6(4)\cdot10^{-3}$, $2.1(3)\cdot10^{-3}$ and $1.9(6)\cdot10^{-3}$ GPa^{-1}, respectively; whereas for the case of our calculations the obtained values for the compressibilities are $3.7(4)\cdot10^{-3}$, $2.0(5)\cdot10^{-3}$ and $1.8(3)\cdot10^{-3}$ GPa^{-1}. These experimental (theoretical) results indicate that around 42% (43%) of the total compression at room pressure is being accommodated along the direction of maximum compressibility. Taking into account the eigenvector ev_1, the major compression direction at zero pressure occurs in the (010) plane at the given angle Ψ (see **Tables S9 and S10**) relative to the *c*-axis (from ***c*** to ***a***) or equivalently at an angle θ relative to the *a*-axis (from *a* to *c*). In particular, the experimental major compression direction at room pressure is at $\theta = -19(5)^{o}$ from the *a*-axis whereas for our calculations is at -17(3)º from the *a*-axis. The experimental direction of intermediate compressibility at room pressure, given by eigenvector ev_2, is in the (010) plane perpendicular to the direction of maximum compressibility, and the direction of minimum compressibility at room pressure, given by eigenvector ev_3, is along the *b* axis. On the other hand, in base of our *ab initio* calculations, the direction of intermediate compressibility at room pressure is along the *b*-axis, and the direction of minimum compressibility at room pressure is in the (0 1 0) plane perpendicular to the direction of maximum compressibility.

As regards the behavior of the experimental and theoretical compressibility tensor under pressure, it is found that $\beta_{11} > \beta_{33} > \beta_{22}$ is maintained as pressure increases. This result shows that a greater compressibility along the *a*-axis is found under pressure and that *b*-axis is the one that undergoes less compression. The experimental (theoretical) compressibility along the *a*-axis, β_{11}, increases slightly (does not change) under pressure. The compressibilities along *b*-axis and *c*-axis, β_{22} and β_{33}, decrease as pressure increases.

The experimental (theoretical) maximum compressibility, λ_1, varies slightly (increases slightly) under compression. The intermediate and minimum compressibility, λ_2 and λ_3, decrease with pressure. Under compression, the experimental (theoretical) direction of maximum compressibility, θ, approaches (moves away slightly) the *a*-axis. In both cases, the direction of maximum compressibility under pressure is always closer to the *a*-axis than to the *c*-axis. To conclude, the experimental and theoretical direction of intermediate compressibility under pressure is in the (010) plane perpendicular to the direction of maximum compressibility, and the direction of minimum compressibility is along the *b*-axis.

Table S9. Experimental isothermal compressibility tensor coefficients, β_{ij}, and their eigenvalues, λ_i, and eigenvectors, ev_i, for B-type Tb_2O_3 at several pressures. The results are given using the finite Eulerian method. The eigenvalues are given in decreasing value long a column.

P(GPa)	0.0	2.0	4.0	6.0	8.0	10.0	11.0
β_{11} (10^{-3} GPa^{-1})	3.2(3)	3.2(3)	3.2(3)	3.3(3)	3.3(3)	3.3(3)	3.3(3)
β_{22} (10^{-3} GPa^{-1})	1.9(6)	1.2(6)	0.8(6)	0.7(6)	0.5(6)	0.4(6)	0.4(6)
β_{33} (10^{-3} GPa^{-1})	2.5(3)	2.2(3)	2.0(3)	1.8(3)	1.7(3)	1.6(3)	1.5(3)
β_{13} (10^{-3} GPa^{-1})	-0.62(12)	-0.65(11)	-0.68(11)	-0.71(11)	-0.73(11)	-0.75(11)	-0.76(11)
λ_1 (10^{-3} GPa^{-1})	3.6(4)	3.5(3)	3.5(3)	3.6(3)	3.6(3)	3.6(3)	3.6(3)
ev_1 (λ_1)	(0.87,0,-0.49)	(0.90,0,-0.44)	(0.91,0,-0.40)	(0.92,0,-0.38)	(0.93,0,-0.36)	(0.94,0,-0.35)	(0.94,0,-0.34)
λ_2 (10^{-3} GPa^{-1})	2.1(3)	1.9(3)	1.7(3)	1.5(3)	1.4(3)	1.3(3)	1.2(3)
ev_2 (λ_2)	(0.49,0,0.87)	(0.44,0,0.90)	(0.40,0,0.91)	(0.38,0,0.92)	(0.36,0,0.93)	(0.35,0,0.94)	(0.34,0,0.94)
λ_3 (10^{-3} GPa^{-1})	1.9(6)	1.2(6)	0.8(6)	0.7(6)	0.5(6)	0.4(6)	0.4(6)
ev_3 (λ_3)	(0,1,0)	(0,1,0)	(0,1,0)	(0,1,0)	(0,1,0)	(0,1,0)	(0,1,0)
Ψ, θ(°)[a]	119(5), -19(5)	116(5), -16(5)	114(4), -14(4)	112(4), -13(4)	111(4), -12(4)	110(3), -11(3)	110(3), -11(3)

[a] The major compression direction occurs in the (0 1 0) plane at the given angles Ψ to the *c*-axis (from *c* to *a*) and θ to the *a*-axis (from *a* to *c*).

Table S10. Theoretical isothermal compressibility tensor coefficients, β_{ij}, and their eigenvalues, λ_i, and eigenvectors, ev_i, for B-type Tb_2O_3 at several pressures. The results are given using the finite Eulerian method. The eigenvalues are given in decreasing value along a column.

P(GPa)	0.0	2.0	4.0	6.0	8.0	10.0	11.0
β_{11} (10^{-3} GPa^{-1})	3.3(3)	3.3(3)	3.3(3)	3.3(3)	3.3(3)	3.3(3)	3.3(3)
β_{22} (10^{-3} GPa^{-1})	2.0(4)	1.6(4)	1.2(4)	1.0(4)	0.8(4)	0.7(4)	0.7(4)
β_{33} (10^{-3} GPa^{-1})	2.2(3)	2.08(22)	2.02(22)	1.96(22)	1.90(22)	1.85(21)	1.82(18)
β_{13} (10^{-3} GPa^{-1})	-0.77(9)	-0.81(9)	-0.85(9)	-0.91(9)	-0.97(9)	-1.05(10)	-1.09(8)
λ_1 (10^{-3} GPa^{-1})	3.7(4)	3.7(3)	3.7(3)	3.8(3)	3.8(3)	3.9(3)	3.9(4)
ev_1 (λ_1)	(0.89,0,-0.46)	(0.89,0,-0.45)	(0.89,0,-0.45)	(0.89,0,-0.45)	(0.89,0,-0.45)	(0.89,0,-0.46)	(0.89,0,-0.47)
λ_2 (10^{-3} GPa^{-1})	2.0(5)	1.67(19)	1.59(19)	1.50(19)	1.40(18)	1.30(18)	1.25(19)
ev_2 (λ_2)	(0,1,0)	(0.45,0,0.89)	(0.45,0,0.89)	(0.45,0,0.89)	(0.45,0,0.89)	(0.46,0,0.89)	(0.47,0,0.89)
λ_3 (10^{-3} GPa^{-1})	1.8(3)	1.6(4)	1.2(4)	1.0(4)	0.8(4)	0.7(4)	0.7(4)
ev_3 (λ_3)	(0.46,0,0.89)	(0,1,0)	(0,1,0)	(0,1,0)	(0,1,0)	(0,1,0)	(0,1,0)
Ψ, θ(°)[a]	117(3), -17(3)	117(3), -17(3)	117(3), -17(3)	116.7(2.4), -16.9(2.4)	117.0(2.2), -17.4(2.2)	117.5(2.1), -18.0(2.1)	117.7(1.8), -18.4(1.8)

[a] The major compression direction occurs in the (0 1 0) plane at the given angles Ψ to the *c*-axis (from *c* to *a*) and θ to the *a*-axis (from *a* to *c*).

References

[1] T. Danno, D. Nakatsuka, Y. Kusano, H. Asaoka, M. Nakanishi, T. Fujii, Y. Ikeda, J. Takada, Crystal Structure of β-Fe_2O_3 and Topotactic Phase Transformation to α-Fe_2O_3. Cryst. Growth Des. **2013**, *13*, 770-774.

[2] T. Yamanaka, T. Nagai, T. Okada and T. Fukuda, Structure Change of Mn_2O_3 under High Pressure and Pressure-Induced Transition. Z. Kristallogr. **2005**, *220*, 938–945.

[3] H. Yusa, T. Tsuchiya, N. Sata, and Y. Ohishi, High-Pressure Phase Transition to the Gd_2S_3 Structure in Sc_2O_3: A New Trend in Dense Structures in Sesquioxides. Inorg. Chem. **2009**, *48*, 7537–7543.

[4] D. Liu, W.W. Lei, Y.W. Li, Y.M. Ma, J. Hao, X.H. Chen, Y.X. Jin, D. Liu, S.D. Yu, Q.L. Cui, and G.T. Zou, High-Pressure Structural Transitions of Sc_2O_3 by X-Ray Diffraction, Raman Spectra, and Ab Initio Calculations. Inorg. Chem. **2009**, *48*, 8251–8256.

[5] S.V. Ovsyannikov, E. Bykova, M. Bykov, M.D. Wenz, A.S. Pakhomova, K. Glazyrin, H.-P. Liermann, and L. Dubrovinsky, Structural and Vibrational Properties of Single Crystals of Scandia, Sc_2O_3 under High Pressure. J. Appl. Phys. **2015**, *118*, 165901.

[6] D. Liu, W. W. Lei, B. Zou, S. D. Yu, J. Hao, K. Wang, B. B. Liu, Q. L. Cui, and G. T. Zou, High-Pressure x-Ray Diffraction and Raman Spectra Study of Indium Oxide. J. Appl. Phys. **2008**, *104*, 083506.

[7] J. Qi, J. F. Liu, Y. He, W. Chen, and C. Wang, Compression Behavior and Phase Transition of Cubic In_2O_3 Nanocrystals. J. Appl. Phys. **2011**, *109*, 063520.

[8] B. Garcia-Domene, H. M. Ortiz, O. Gomis, J. A. Sans, F. J. Manjón, A. Muñoz, P. Rodríıguez-Hernández, S. N. Achary, D. Errandonea, D. Martíınez-García, A. H. Romero, A. Singhal, and A. K. Tyagi, High-Pressure Lattice Dynamical Study of Bulk and Nanocrystalline In_2O_3. J. Appl. Phys. **2012**, *112*, 123511.

[9] S. Jiang, J. Liu, C.L. Lin, L.G. Bai, W.S. Xiao, Y.F. Zhang, D.C. Zhang, X.D. Li, Y.C. Li, and L.Y. Tang, Pressure-induced phase transition in cubic Lu_2O_3. J. Appl. Phys. **2010**, *108*, 083541.

[10] C.-M. Lin, K.-T. Wu, T.-L. Hung, H.-S. Sheu, M.-H. Tsai, J.-F. Lee, and J.-J. Lee, Phase Transitions in Lu_2O_3 under High Pressure. Solid State Commun. **2010**, *150*, 1564-1569.

[11] J.P. McClure, High Pressure Phase Transistions in the Lanthanide Sesquioxides. Ph. D. Thesis, University of Nevada, Las Vegas (2009).

[12] C. Meyer, J. P. Sanchez, J. Thomasson, and J. P. Itié, Mössbauer and Energy-Dispersive x-Ray-Diffraction Studies of the Pressure-Induced Crystallographic Phase Transition in C-Type $Yb2O_3$. Phys. Rev. B **1995**, *51*, 12187-12193.

[13] K. A. Irshad, P. Anees, S. Sahoo, N. R. Sanjay Kumar, V. Srihari, S. Kalavathi, and N. V. Chandra Shekar, Pressure Induced Structural Phase Transition in Rare Earth Sesquioxide Tm_2O_3: Experiment and Ab Initio Calculations. J. Appl. Phys. **2018**, *124*, 155901.

[14] O. Gomis, D. Santamaría-Pérez, J. Ruiz-Fuertes, J.A. Sans, R. Vilaplana, H.M. Ortiz, B. García-Domene, F. J. Manjón, D. Errandonea, P. Rodríguez-Hernández, A. Muñoz, and M. Mollar, High-Pressure Structural and Elastic Properties of Tl_2O_3. J. Appl. Phys. **2014**, *116*, 133521.

[15] Q.X. Guo, Y.S. Zhao, C. Jiang, W.L. Mao, Z.W. Wang, J.Z. Zhang and Y.J. Wang, Pressure-Induced Cubic to Monoclinic Phase Transformation in Erbium Sesquioxide Er_2O_3. Inorg. Chem. **2007**, *46*, 6164–6169.

[16] X.T. Ren, X.Z. Yan, Z.H. Yu, W.T. Li, L. Wang, Photoluminescence and Phase Transition in Er_2O_3 under High Pressure. J. Alloys & Comp. **2017**, *725*, 941.

[17] H. Yusa, T. Tsuchiya, N. Sata and Y. Ohishi, Dense Yttria Phase Eclipsing the A-Type Sesquioxide Structure: High-Pressure Experiments and ab initio Calculations. Inorg. Chem. **2010**, *49*, 4478-4485.
[18] Q. Zhang, X. Wu, and S. Qin, Pressure-induced phase transition of B-type Y_2O_3. Chin. Phys. B **2017**, *26*, 090703.
[19] S. Jiang, J. Liu, X.D. Li, L.G. Bai, W.S. Xiao, Y.F. Zhang, C.L. Lin, Y.C. Li, and L.Y. Tang, Phase transformation of Ho_2O_3 at high pressure. J. Appl. Phys. **2011**, *110*, 013526.
[20] K.A. Irshad, N.V. Chandra Shekar, V. Srihari, K.K. Pandey, S. Kalavathi, High Pressure Structural Phase Transitions in Ho: Eu_2O_3. J. Alloys & Comp. **2017**, *725*, 911-915.
[21] S. Jiang, J. Liu, C.L. Lin, L.G. Bai, Y.F. Zhang, X.D. Li, Y.C. Li, L.Y. Tang, H. Wang, Structural Transformations in Cubic Dy_2O_3 at High Pressures. Solid State Commun. **2013**, *169*, 37–41.
[22] F. X. Zhang, M. Lang, J. W. Wang, U. Becker, and R. C. Ewing, Structural Phase Transitions of Cubic Gd_2O_3 at High Pressures. Phys. Rev. B **2008**, *78*, 064114.
[23] L.G. Bai, J. Liu, X.D. Li, S. Jiang, W.S. Xiao, Y.C. Li, L.Y. Tang, Y.F. Zhang, and D.C. Zhang, Pressure-Induced Phase Transformations in Cubic Gd_2O_3. J. Appl. Phys. **2009**, *106*, 073507.
[24] X. Zou, C. Gong, B.B. Liu, Q.J. Li, Z.P. Li, B. Liu, R. Liu, J. Liu, Z.Q. Chen, B. Zou, T. Cui, X. Bai, and H.W. Song, X-Ray Diffraction of Cubic Gd_2O_3/Er under High Pressure. Phys. Stat. Sol. (b) **2011**, *248*, 1123–1127.
[25] S. Jiang, L.G. Bai, J. Liu, W.S. Xiao, X.D. Li, Y.C. Li, L.Y. Tang, Y.F. Zhang, D.C. Zhang, L.R. Zheng, The Phase Transition of Eu_2O_3 under High Pressures. Chin. Phys. Lett. **2009**, *26*, 076101.
[26] G. Chen, J. R. Peterson, and K.E. Brister, An Energy-Dispersive X-Ray Diffraction Study of Monoclinic Eu_2O_3 under Pressure. J. Solid State Chem. **1994**, *111*, 437-439.
[27] Q.X. Guo, Y.S. Zhao, C. Jiang, W.L. Mao, and Z.W. Wang, Phase Transformation in Sm_2O_3 at High Pressure: In Situ Synchrotron X-Ray Diffraction Study and Ab Initio DFT Calculation. Solid State Commun. **2008**, *145*, 250-254.
[28] S. Jiang, J. Liu, C.L. Lin, X.D. Li, and Y.Ch. Li, High-Pressure x-Ray Diffraction and Raman Spectroscopy of Phase Transitions in Sm_2O_3. J. Appl. Phys. **2013**, *113*, 113502.
[29] K. K. Pandey, N. Garg, A. K. Mishra, and S. M. Sharma, High pressure phase transition in Nd_2O_3. J. Phys.: Conf. Series **2012**, *377*, 012006.
[30] S. Jiang, J. Liu, L.G. Bai, X.D. Li, Y.ch. Li, S.M. He, S. Yan, and D.X. Liang, Anomalous Compression Behaviour in Nd_2O_3 Studied by X-Ray Diffraction and Raman Spectroscopy. AIP Adv. **2018**, *8*, 025019.
[31] M. J. Lipp, J. R. Jeffries, H. Cynn, J. H. Park Klepeis, W. J. Evans, D. R. Mortensen, G. T. Seidler, Y. Xiao, and P. Chow, Comparison of the high-pressure behavior of the cerium oxides Ce_2O_3 and CeO_2. Phys. Rev. B **2016**, *93*, 064106.
[32] A.K. Pathak and T. Vazhappily, Ab Initio Study on Structure, Elastic, and Mechanical Properties of Lanthanide Sesquioxides. Phys. Stat. Sol. (b) **2018**, *255*, 1700668.
[33] B. Wu, M. Zinkevich, F. Aldinger, D.Z. Wen, L. Chen, Ab Initio Study on Structure and Phase Transition of A- and B-Type Rare-Earth Sesquioxides Ln_2O_3 (Ln=La-Lu, Y, and Sc) Based on Density Function Theory. J. Solid State Chem. **2007**, *180*, 3280-3287.
[34] D. Richard, L.A. Errico, and M. Rentería, Structural Properties and the Pressure-Induced C → A Phase Transition of Lanthanide Sesquioxides from DFT and DFT + U Calculations. J. Alloys Compd. **2016**, *664*, 580-589.
[35] E. Husson, C. Proust, P. Gillet, and J.P. Itié, Phase Transitions in Yttrium Oxide at High Pressure Studied by Raman Spectroscopy. Mater. Res. Bull. **1999**, *34*, 2085-2092.

[36] T. Ogawa, N. Otani, T. Yokoi, C.A.J. Fisher, A. Kuwabara, H. Moriwake, M. Yoshiya, S. Kitaoka, M. Takata, Density Functional Study of the Phase Stability and Raman Spectra of Yb_2O_3, Yb_2SiO_5 and $Yb_2Si_2O_7$ under Pressure. Phys. Chem. Chem. Phys. **2018**, *20*, 16518-16527.

[37] T. Hongo, K. Kondo, K.G. Nakamura, T. Atou, High Pressure Raman Spectroscopic Study of Structural Phase Transition in Samarium Oxide. J. Mater. Sci. **2007**, *42*, 2582-2585.

[38] J. Zarembowitch, J. Gouteron, A. M. Lejus, Raman Spectra of Lanthanide Sesquioxide Single Crystals with A-Type Structure. Phys. Stat. Sol. (b) **1979**, *94*, 249-256.

[39] D. Avisar and T. Livneh, The Raman-Scattering of A-Type Ce_2O_3. Vibrat. Spec. **2016**, *86*, 14-16.

[40] P. Canepa, R.M. Hanson, P. Ugliengo, M. Alfredsson, J-ICE: A New Jmol Interface for Handling and Visualizing Crystallographic and Electronic Properties. J. Appl. Crystallogr. **2011**, *44*, 225−229.

[41] S. Haussühl, Physical Properties of Crystals. An Introduction (Wiley-VCH, Weinheim, 2007).

[42] R. J. Angel, http://www.rossangel.com/text_strain.htm